In Situ Detection of Inclusions in Liquid Metals: Part II. Metallurgical Applications of LiMCA Systems

RODERICK I.L. GUTHRIE and MEI LI

The study of the performance of the probes in the water-based Aqueous Particle Sensor II (APS II) and the metal-based Liquid Metal Cleanliness Analyzer (LiMCA) systems employing the mathematical model developed in Part I shows that the currently used parabolically shaped orifice is favorable for particle detection by providing a uniform and stable flow field and a parallel distributed electric current at the throat of the orifice. Combined with the Ohmic model of the electric sensing zone (ESZ), which correlates the ESZ resistance change with particle position within the ESZ, the model predicts that larger particles have longer transient times than do smaller ones, that less denser particles have shorter transient times than do more denser particles of the same size in water and metal based LiMCA systems. Differences in transient times become more pronounced the larger the inclusions, in keeping with experimental data. In the metal-based LiMCA system, conducting and nonconducting inclusions can be readily discriminated from one another as they generate negative and positive peak signals, respectively. The results prove that inclusion discrimination on the basis of particle density difference is realizable in a water-based LiMCA system and, from a theoretical standpoint, that particles of different density and conductivity in molten metals are potentially distinguishable with a LiMCA system using digital signal processing (DSP) technology. The APS II system has been successfully used in the physical modeling of some metallurgical operations and the LiMCA system in a broad range of applications in various molten metals.

I. INTRODUCTION

THE previous article (Part I) described the electric sensing zone (ESZ) principle,[1] an Ohmic model,[2] and a mathematical model for studying the electromagnetic fields, fluid flow, and particle behavior within the Liquid Metal Cleanliness Analyzer (LiMCA) system. In the present article, a water-based version of LiMCA system known as the Aqueous Particle Sensor II (APS II) system[3] and a metal-based LiMCA system are first described. The performance of the probes is evaluated based on the predicted electromagnetic and fluid flow fields, as well as pass-through fractions of particles within the ESZ using the mathematical model developed in Part I. The electric circuit of the LiMCA system used at McGill University for particle detection in molten metals is analyzed. Then, the applications of the APS II system in water modeling of inclusion distributions in stirred ladles, inclusion float out in steelmaking tundishes, submerged powder injection in the refining and alloying of melts, and inclusion type discrimination using digital signal processing (DSP) technology[41] are presented. Finally, typical metallurgical applications of LiMCA in molten metals are described, and the knowledge gained as a result of this novel technology is assessed.

RODERICK I.L. GUTHRIE, Macdonald Professor, FRSC, and Director, McGill Metals Processing Center, is with the Department of Mining and Metallurgical Engineering, McGill University, Montreal, PQ, Canada H3A 2B2. MEI LI, formerly Graduate Student, McGill Metals Processing Center, Department of Mining and Metallurgical Engineering, McGill University, is with the Scientific Research Laboratory, Ford Motor Company, Dearborn, MI 48121-2053.

Manuscript submitted November 16, 2000.

II. WATER BASED AND METAL BASED LiMCA SYSTEMS

A. *Water-based LiMCA System—APS II System*

A schematic experimental setup of the APS II system is shown in Figure 1. The probe of the APS II system used to model the metal-based LiMCA probe is designed on a one-to-one scale to ensure geometrical similarity. The shape of the orifices is parabolic and could be represented as

$$y = 10^{-3} * x^2 + R \qquad [1]$$

where R is the radius at the throat of the circular orifice ($\sim$150 μm), and x and y are the axial and radial coordinates, respectively, in micrometer (Figure 2(a) in Part I). The probe head essentially consists of the electrically insulating sampling tube and two concentric electrodes. The inner concentric electrode is press-fixed to the interior of the tube, while the outer concentric electrode surrounds the tube leaving a small gap around the orifice to allow water to pass into it. By alternate use of moderate vacuum and pressure, aqueous samples are aspirated into and, then, exhausted from the sampling tube through the orifice, *i.e.*, the ESZ. To minimize the generation of electrical noise, two venturi tubes are connected in parallel to generate the vacuum needed for air aspiration. The level of vacuum within the probe could be controlled by increasing, or decreasing, the flow rate of air through the venturi tubes, which in turn determined the sampling flow rate. Compressed gas is used to cycle pressure inside the probe tube. The APS II system amplifier is designed to maintain a constant potential across the orifice (12 V), irrespective of the electrical conductivity of the water used, and by implication, its temperature. When a particle passes through the ESZ, the voltage signal is amplified by

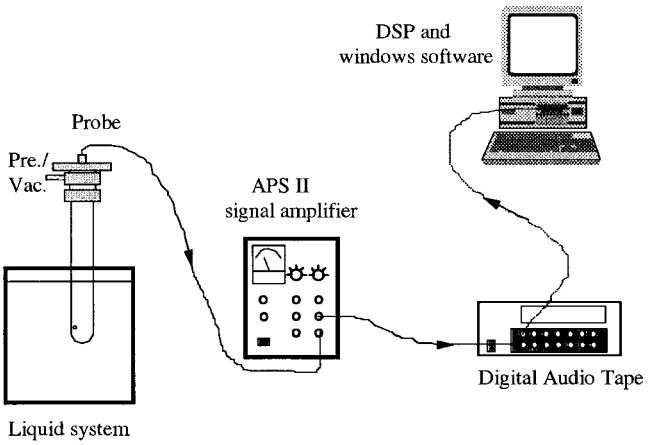

Fig. 1—Schematic experimental setup of APS II system.

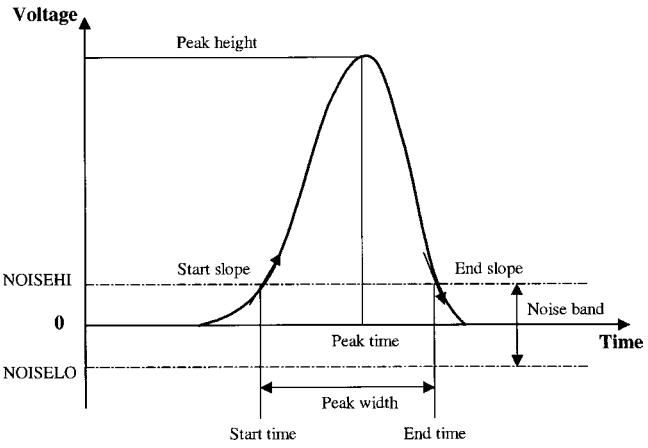

Fig. 2—The seven peak parameters generated by DSP in LiMCA system.

the APS II system and, simultaneously, sent to the oscilloscope and digital audio tape (DAT). The oscilloscope is used to display the signals and the DAT recorder is used to record the incoming signals. The recorded data on the DAT tape are subsequently sent to the computer, which digitizes and analyzes the signals using a custom designed DSP program that passes the process information onto a Windows-based software program, METALWINDOWS*. In the DSP analysis step, seven characteristic parameters are generated for every signal. These comprise pulse height, pulse width, start slope, end slope, time to pulse peak, start time, and end time (Figure 2). It is noted that all these parameters are dependent on the noise thresholds set, *i.e.*, NOISEHI and NOISELO, which mark the margins of the noise band of the signal. The noise band reflects the operational conditions and determines the minimum size of the particles that the system can detect under such conditions.

*METALWINDOWS is a trademark of McGill Metals Processing Center.

B. *Metal-based LiMCA System*

A schematic of the metal-based LiMCA system is shown in Figure 3. The primary difficulty in developing an ESZ device for molten metals, when compared with aqueous electrolytes, is their very low electrical resistivity (~1,000,000

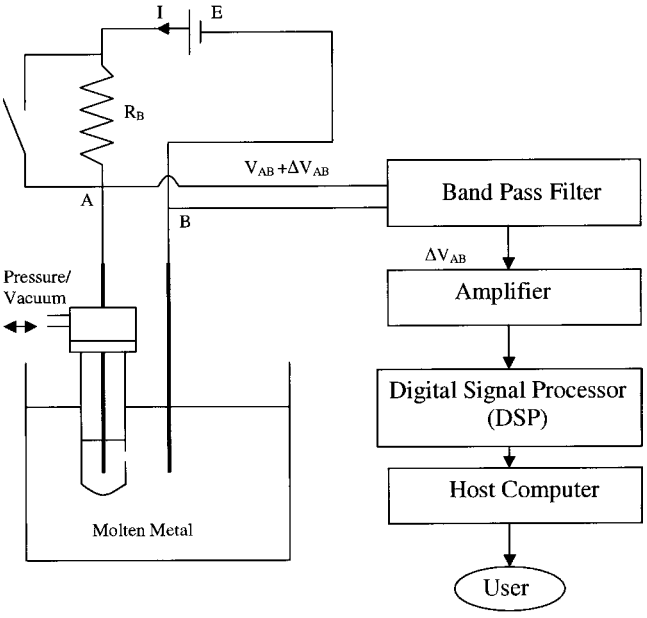

Fig. 3—Schematic configuration of DSP-based LiMCA system.

times lower), which renders the resistance changes caused by particles displacing the fluid within the orifice and given by Eq. [7] in Part I, extremely small. To obtain measurable voltage pulses, the circuit current compared with aqueous ESZ systems has to be increased significantly (60 A *vs* 1 mA), while the threshold pulse height for particle detection has to be greatly lowered by reducing the inevitable background noise on the reference baseline as far as possible. This is accomplished through the use of sensitive electronics and by electromagnetic shielding and appropriate grounding of circuit components. In applying LiMCA to high melting point, reactive metals, such as aluminum, magnesium, copper, and steel alloys, the electrical circuit design is essentially the same, but new probes have to be developed for each metal. The resistance to thermal shock, chemical wear, and electrical insulation of sampling tubes, as well as dimensional stability of the ESZ orifice, all have to be considered and optimized according to the melt being sampled.

1. *Analysis of LiMCA's electric circuit*

As shown in Figure 3, a direct current (DC) battery with an electromotive force, E, drives a ripple free current, I, while a ballast resistance, R_B, regulates this current. The transient voltage pulses, ΔV_{AB}, caused by the passage of particles, riding on a steady potential difference, V_{AB}, across the ESZ are detected at the ends of feeder electrodes A and B. The value of this voltage pulse is the product of the change in resistance, ΔR caused by the passage of an inclusion through the ESZ and the electric current, I. The pulse is also a function of the ballast resistance, as the following derivation shows.[5] Referring to Figure 3,

$$V_{AB} = \frac{R_{AB}}{R_{AB} + R_B} \cdot E \qquad [2]$$

$$\Delta V_{AB} = \left(\frac{\partial V_{AB}}{\partial R_{AB}}\right) \cdot \Delta R_{AB} = \frac{(R_{AB} + R_B) - R_{AB}}{(R_{AB} + R_B)^2} \cdot E \cdot \Delta R_{AB} \qquad [3]$$

since

$$I_0 = \frac{E}{R_{AB} + R_B} \quad [4]$$

then

$$\Delta V_{AB} = \frac{R_{AB}}{R_{AB} + R_B} \cdot \Delta R_{AB} \cdot I_0 \quad [5]$$

where I_0 is the current passing through the orifice in the absence of a particle in the ESZ. For cases where the ballast resistance, R_B, is much greater than the electrodes resistance plus the orifice resistance, R_{AB}, this expression simplifies to

$$\Delta V_{AB} = I_0 \cdot \Delta R_{AB} = \frac{4\rho_e I d^3}{\pi D^4} \quad [6]$$

If particle size, d, is not small compared to the orifice diameter, D, ΔR_{AB} is increased through distortion of the electric field flowing between the cylindrical walls of the ESZ and the spherical inclusion and needs to be modified by a factor, $f(d/D)$, in Eq. [6][6] giving

$$\Delta V_{AB} = \frac{4\rho_e I d^3}{\pi D^4} f(d/D) \quad [7]$$

The $f(d/D)$ was obtained according to the numerical results of Smythe[7] in analyzing ideal fluid flow around a sphere in a circular tube and can be expressed as:[8]

$$f(d/D) = [1 - 0.8\ (d/D)^3]^{-1} \quad [8]$$

2. *LiMCA probes for molten aluminum, magnesium, copper, and steel*

For applications in aluminum, heat resistant borosilicate and alumino-silicate glass sampling tubes are used, while the electrodes can be made from mild steel or tungsten. For copper-beryllium alloys, irons and transformer steel melts, quartz, as well as boron-nitride sampling tubes, have proved successful. For liquid magnesium and oxygen bearing copper melts, a concentric steel tube probe (CSTP) has recently been developed that resolves chemical attack problems with quartz tubes. Quartz tubes are chemically reduced in molten aluminum and magnesium, leading to erosion and expansion of the ESZ region. By comparison, both borosilicate and alumino-silicate probes resist chemical attack by molten aluminum and its alloys, the latter being favored in practice, owing to its higher softening point. Figure 4 shows the scanning electron micrographs of an orifice in a borosilicate (KIMAX) tube before and after 90 minutes of use in aluminum at 710 °C. It can be seen that although some surface erosion has occurred, there are no major changes in either the shape or the dimensions of the orifice.

(*a*)

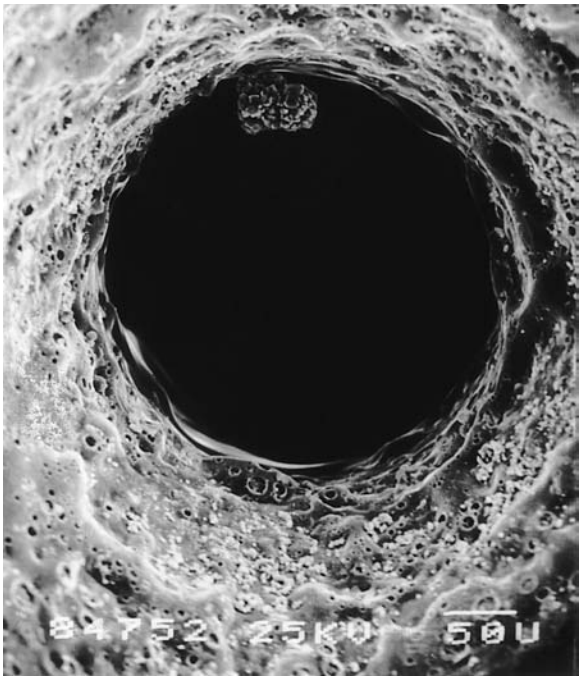

(*b*)

Fig. 4—Scanning electron micrographs of an orifice in a borosilicate (KIMAX) tube (*a*) before use and (*b*) after 90 min of use in molten aluminum at 710 °C.

III. METALLURGICAL APPLICATIONS OF THE APS II SYSTEM

The APS II system has been a great help for studying inclusion behavior in metallurgical processing vessels. It allows metal quality measurements to be made *in situ* during the physical modeling of complicated metallurgical processes. These measurements also help to test the validity of the various mathematical models. Four examples are presented in this section, one deals with inclusion distributions in stirred ladles,[9] another considers the floatation of alumina inclusions from liquid steel flowing through tundishes,[10] the third concerns particle behavior during the powder injection,[11] and the fourth considers the feasibility of inclusion type discrimination using DSP technology in APS II system.

A. *Study of Inclusion Distribution in Stirred Ladles*

A one-fifth scale water model of a 150 ton steelworks ladle was stirred by gas from a submerged, centrally located

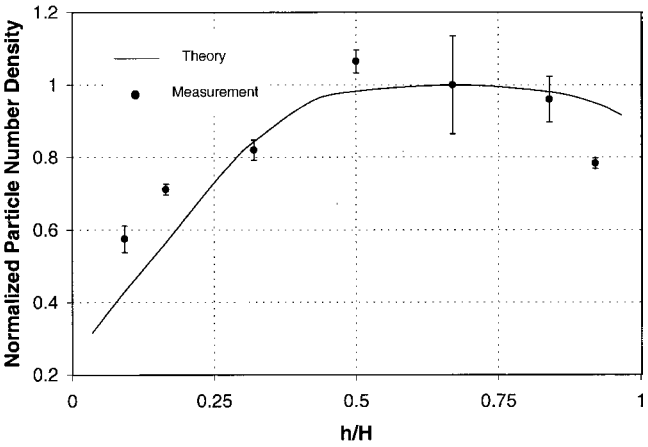

Fig. 5—Comparison of experimentally measured and predicted normalized particle number density *vs* distance from the bottom of a model ladle (*H* is the height of the ladle).

orifice, and nonmetallic hollow glass microspheres having a specific gravity of 0.2 g/cm^3 were added. The measurement of the number and size distribution of inclusions at different locations within the ladle was carried out with the APS II system. The measured results are consistent with the predictions of the numerical model that solved the relevant equations for continuity, motion, and turbulence for axisymmetric flow in stirred ladles in conjunction with a mass conservation equation for nonreacting, monosized inclusions entrained within this recirculating flow. As an example, Figure 5 shows the predicted normalized particle number density distribution along a vertical axis of the ladle, $r/R_{\text{ladle}} = 0.5625$, where r is the radial coordinate, and R_{ladle} is the radius of the ladle, and the corresponding experimental results. The Stokes rising velocity is 3×10^{-3} m/s, and the gas volumetric flow rate is 4.167×10^{-5} m^3/s. One sees that the liquid steel deeper within the ladle, closer to the rising plume, is significantly cleaner than the liquid closer to the surface.

B. *Study of Particle Separation in Tundish in Steelmaking*

In modeling the behavior of inclusions in liquid steel, the species conservation equation was solved where a vertical-velocity component was ascribed to the inclusions equal to their Stokes rising velocity. The experimental measurement of the number and size distribution of inclusions was performed with the APS II system. For stimulating actual inclusions in molten steel, hollow glass microspheres over the size range of 20 to 110 μm diameter were fed continuously at a feeding rate of 0.5 L/min into a full scale water model of Stelco's Lake Eric 70 tonne tundish through the inlet shroud. The specific density of these microspheres was 295 kg/m^3. Clearly one is interested in minimizing the number of inclusions entrained into the mold through the outlet nozzle, N_{out}, *vs* the number of inclusions entering the tundish, N_{in}. Defining the residual ratio as $N_{\text{out}}/N_{\text{in}}$, where N represents a number density of inclusions per unit volume. Figure 6 shows that the computed ratios are consistent with measured ratios. As seen, at time zero, there are no inclusions within the tundish, but these gradually build up until a steady-state condition is reached, corresponding to about three mean residence times. It can also be seen that the higher the Stokes

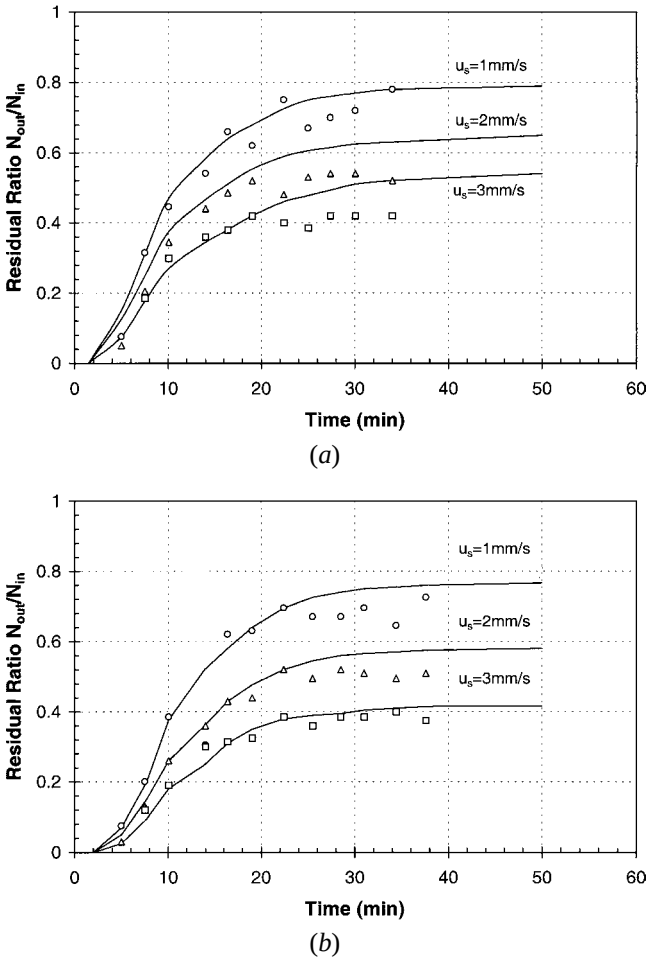

Fig. 6—Comparison of experimentally measured and predicted particle separation ratio *vs* time of casting for the single-strand water model tundish: (*a*) without flow control and (*b*) with flow control.

rising velocity of the inclusions, u_s, the lower is the ratio of $N_{\text{out}}/N_{\text{in}}$. Thus, for $u_s = 3$ mm/s, about 40 pct of the incoming inclusions go through the exit ports into the molds.

C. *Study of Powder Injection Processes*

The APS II system can also be used to determine the critical distance in water modeling of powder injection processes, the disengagement distance, $J_{\max}$, which represents the maximum penetration of the three-phase (gas + liquid + particle) jet into the liquid. When the jet reaches this distance, the gas phase breaks up into smaller bubbles that rise to the surface, while the particles decouple and continue to descend on account of their larger momentum. When the probe was set just below the maximum gas-particle penetration distance (particle-liquid zone), after completion of the injection period, the APS II signals diminished. This represents particles settling. However, when the APS II probe was raised to just above $J_{\max}$ distance (gas-particle-liquid zone), after completion of the injection period, large pulses took place.

In the bubbling type of powder injection regime, it was observed during flow visualization that large gas bubbles were forming at the lance tip and that particles were penetrating the bubble gas/liquid interfaces and being dispersed into the liquid. To determine whether the particles entrain any

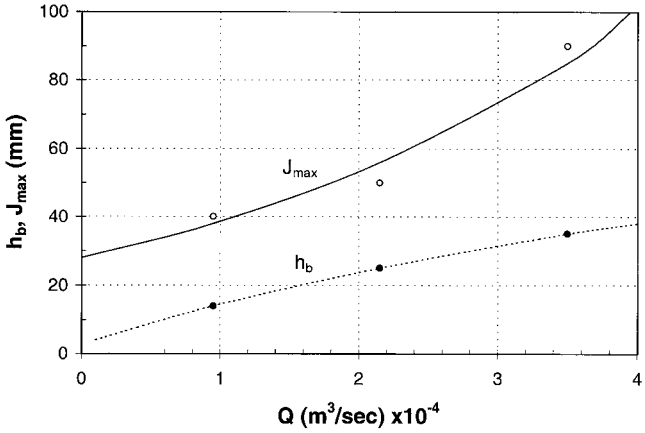

Fig. 7—Comparison of the measured gas-particle disengagement distance, J_{max}, with estimated maximum bubble penetration distance, h_b, in water modeling of powder injection in the bubbling regime.

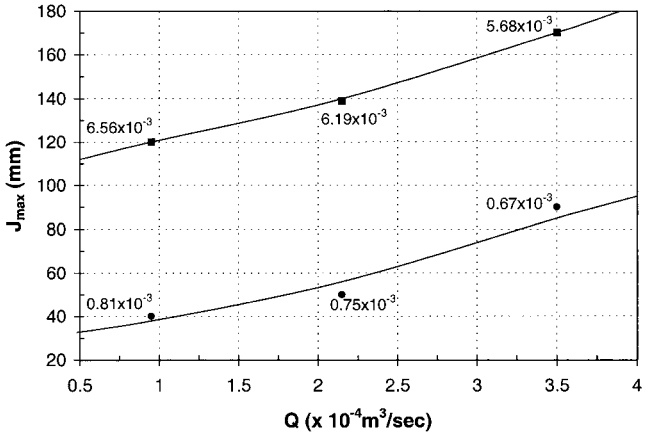

Fig. 8—Measured gas-particle disengagement distance as a function of gas powder flow rate in water modeling of powder injection. The numbers beside each point are the powder mass flow rates in kg/s (■—jetting regime with high particle-gas loading ratio, and ●—bubbling regime with low particle-gas loading ratio).

gas as they separate from the bubble, bubble penetration distances (h_b) and gas-particle jet disengagement distances (J_{max}) obtained by the APS II system were compared, and the results are shown in Figure 7. As seen in Figure 7, the gas-particle disengagement distance is greater than the bubble penetration distance. This means that some volume of gas is entrained by the particle stream when the particles leave the large gas bubbles at the lance tip, and hence, the gas-particle mixture flowed as a jet into the liquid. It was also observed that the depth at which the gas-particle disengages could be increased by increasing the gas flow rate and/or the powder mass flow rate. For example, in Figure 8, for a gas flow rate of 0.95×10^{-4} m^3/s, and a powder mass flow rate of 0.81×10^{-3} kg/s, the disengagement depth was only 40 mm. Disengagement depth increases from 40 to 90 mm when the gas flow rate increased from 0.95×10^{-4} to 3.5×10^{-4} m^3/s. On the other hand, this 40-mm distance was increased to 120 mm for the same volumetric gas flow rate (0.95×10^{-4} m^3/s) when the mass flow rate was increased to 6.56×10^3 kg/s. Such considerations can be useful, particularly in industrial applications where high gas flow rates are often undesirable as increased flow rates result in slopping and splashing of the melt and droplet entrainment from overlying slags.

D. *Particle Discrimination in APS II System*

Particles of different type affect materials properties differently, therefore, the ability to discriminate particles is a valuable feature for an online particle (inclusion) detection system. Mathematical modeling and experimental studies are used to demonstrate that particle discrimination is realizable in APS II system.

In the particle discrimination tests, orifices with a size of 270 and 320 μm were used. The wall thickness of the sampling tube, L_{tube}, was 1.2 mm. The orifice currents used were 30 and 36 μA, while the noise thresholds were ± 2 and ± 15 mV for 270 and 320 μm diameter orifices, respectively. The effect of liquid acceleration on the relative velocity of the particles was studied by changing the flow rate of liquid through the orifice, which was regulated by applying different levels of vacuum. In order to determine the effect of particle density on the time needed to pass through the orifice, the shapes of the signals were measured for particles of the same size but of varying density. Particles tested included latex, silica, and microbubbles of argon. Their physical properties are listed in Table I of Part I of this series of articles. High-purity argon gas was used to generate the microbubbles, which were injected into water using a fine glass needle. The diameter of the argon bubble was controlled by adjusting the pressure drop across the needle.

Using DSP technology, particle discrimination in LiMCA systems seem to be feasible. For every transient pulse generated when a particle passes through the ESZ, seven parameters are presently used to characterize the pulse (Figure 2). These parameters are related to the motion of the particle, which depends on the physical properties of the particle and the fluid flow conditions within the ESZ. Figure 2 also shows that the transient time of the particles flowing through the ESZ is not the time the particle takes to traverse the physical length of the ESZ, but rather the time it takes to pass through the region where the pulse height generated by the particle is higher than the threshold value. Therefore, a numerical study of particle discrimination was carried out by relating the ESZ resistance change using the Ohmic model (Eq. [24] of Part I) to the motion of the particle inside the ESZ. Figure 9 shows the variation in ESZ resistance as particles of different diameter pass through orifices of 320 μm. It can be seen that larger particles reach the noise threshold resistance further away from the orifice center than do smaller particles. Therefore, smaller particles travel shorter distances when the transient time is measured by APS II system. For example, in the 320 μm orifice, a particle of size 100 μm reaches the noise threshold of 15 mV at 0.305 mm from the center of the orifice, while it is 0.102 mm for a particle of 60 μm. Therefore, the transient time measured for a particle of 60 μm is the time it takes to travel 0.204 mm near the center of the orifice, while for a particle of 100 μm, it is the time to travel 0.610 mm.

To study the particle discrimination numerically, equations for the fluid flow and the motion of particles were solved first for particles of varying density and size flowing through the whole orifice. Then, the transient time (Figure 2) was obtained by considering the noise threshold of the

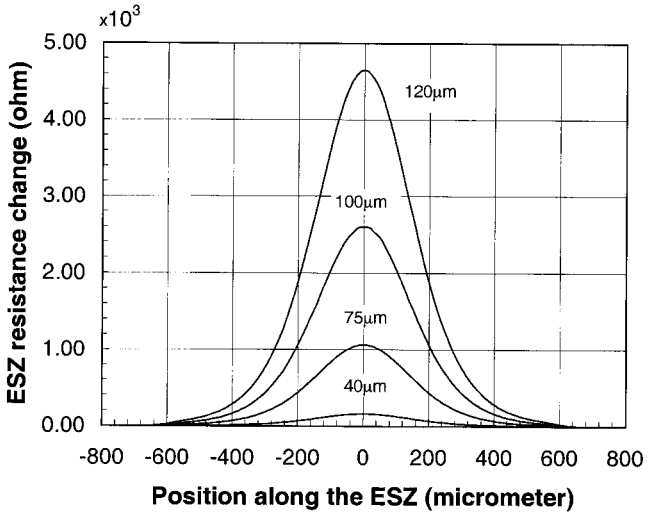

Fig. 9—ESZ resistance change with the position of particles of various diameter in a 320 μm orifice in APS II system.

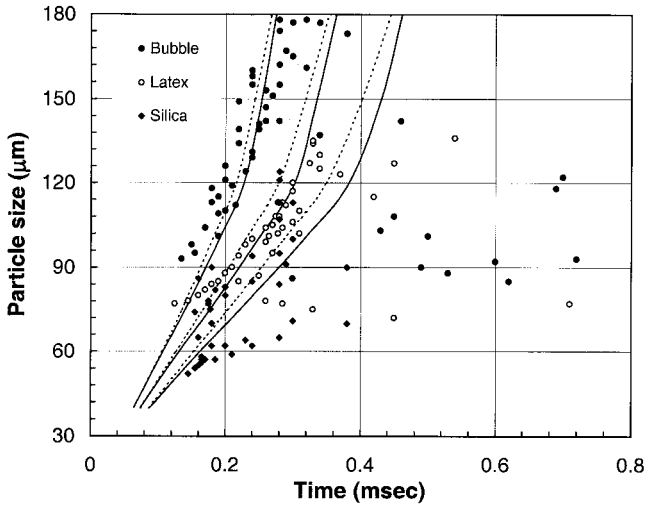

Fig. 10—Comparison of experimentally measured and numerically predicted transient time *vs* particle size in a 270 μm orifice with mean fluid velocity of u_m = 7.4 m/s in APS II system (––– particles flowing into the ESZ along central axis, and ——— particles flowing into the ESZ near wall).

APS II system. The situations studied include a 270 μm orifice with two different mean fluid velocities of 5.63 and 7.4 m/s, and a 320 μm orifice with mean fluid velocity of 7.5 m/s. Predictions on the 270 μm orifice with mean fluid velocity of 7.4 m/s are shown in Figure 10, together with the experimental results.[12]

It can be seen that the agreement between the experimental data and the predictions calculated by the mathematical model was satisfactory. Bubbles were found to have shorter transient times than solid particles of the same size, which can be explained by the different relative velocity developed when they move through the ESZ, as shown in Figure 6 of Part I. Bubbles, which lead the fluid flow, travel faster than the latex microspheres, which are slightly denser than the fluid and follow the fluid flow closely. Silica particles are much denser than the fluid and, thus, lag behind the fluid flow when travelling inside the ESZ, resulting in lower

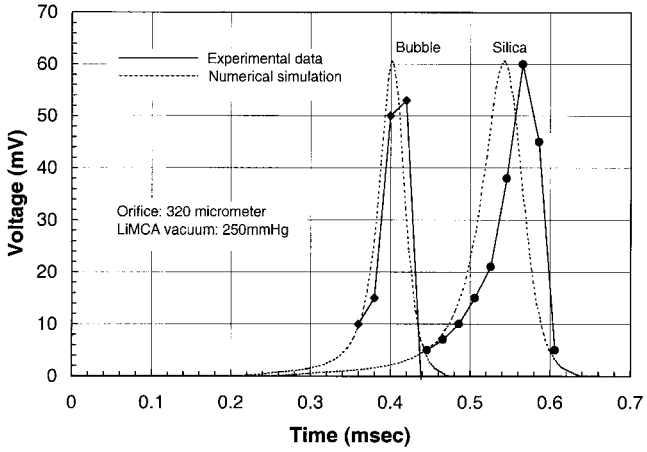

Fig. 11—Comparison of experimentally observed and numerically predicted particle signal shapes generated by different particles using APS II system.

velocity and longer transient time than both latex microspheres and bubbles.

It is also noted from Figure 10 that larger particles have longer transient times than smaller ones of the same density. This is easy to explain for solid particles. For solid particles, the larger the particle, the lower the velocity. On the other hand, for bubbles, the larger the particle, the higher the velocity. It seems that larger bubbles should have shorter transient times than smaller bubbles. In fact, the transient times of larger bubbles, which were measured in APS II system, are longer than smaller bubbles, because larger bubbles reach the threshold voltage for detection much further away from the orifice center, resulting in a longer distance to travel.

Comparing the particle transient time results in a 270 μm orifice with two different mean fluid velocities of 5.63 and 7.4 m/s, it can be seen that the overall transient time decreases as the fluid flow velocity inside the orifice increases. The difference in transient times for bubbles, latex microspheres, and silica particles becomes more significant as particle size increases, improving the discrimination between particles of different densities.

Also shown in Figure 10 are the transient time *vs* particle size for bubbles, latex microspheres, and silica particles flowing into the ESZ from near wall positions (solid lines). The dashed lines are the results for particles flowing into the ESZ along the central axis. The difference between these two situations is not significant, especially for bubbles and small solid particles.

Besides the transient time, on which particle discrimination can be carried out, pulse shape is also characteristic of different particles. Figure 11 shows the observed signal shapes of a typical bubble and silica particle generated in the APS II system,[12] together with the predictions of the numerical simulations (dotted lines). Again, satisfactory agreement was achieved. The bubble, which has a lower density, undergoes acceleration as it approaches the center of the converging ESZ, arriving more rapidly than the silica particle of higher density and inertia, which accelerates more slowly.

Use of the Maxwell model, which allows for distortion of the electric field around inclusions *via* the factor 3/2 of the pure Ohmic model, produces very similar results, but

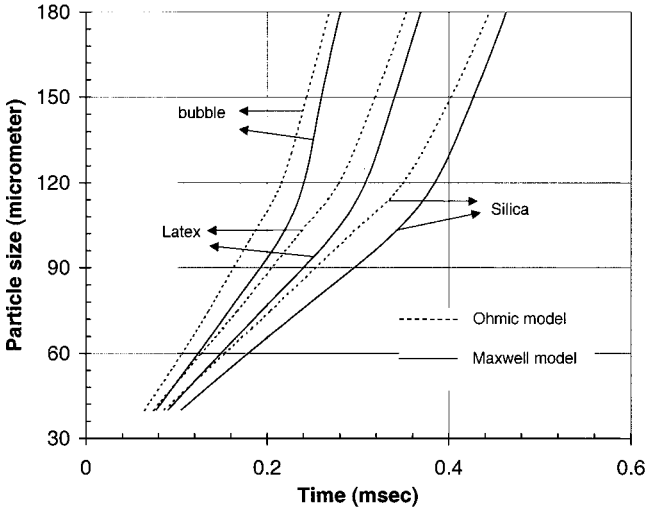

Fig. 12—Comparison of numerically predicted transient time *vs* particle size by the Maxwell model and Ohmic model for particles flowing into the ESZ along the central axis of a 270 μm orifice with mean fluid velocity of u_m = 7.5 m/s in APS II system.

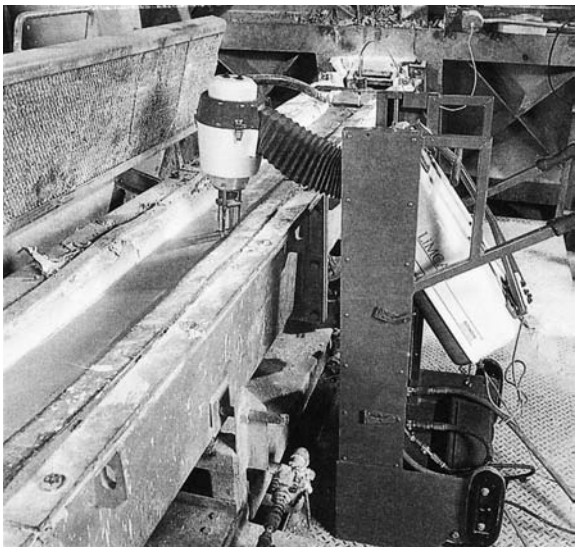

Fig. 13—Schematic illustration of a typical LiMCA II system monitoring the quality of molten aluminum flowing through a launder to a bank of DC casters.

with a slight shift in detection limit, as illustrated in Figure 12.

IV. METALLURGICAL APPLICATIONS OF LiMCA SYSTEM IN MOLTEN METALS

Over the last decade, the LiMCA system has been successfully applied in the aluminum industry in terms of process understanding, control, and optimization and has generated numerous results that were previously unattainable. Typical examples are evaluations of the impact of various alloying methods on metal cleanliness,[13] the optimization of settling times during furnace preparations for direct chill (DC) casting machines,[13,14,15] the evaluation of inclusion removal performance of commercial filters and degassers,[16–22] studies into the effects of metal level variations in the launder on metal cleanliness,[13] and the demonstration of the critical need for proper metal flow control during casting operations.[13,20] The LiMCA II machines[22] produced by Bomem (Quebec City, Canada) are now used worldwide to monitor the numbers of inclusions in liquid aluminum flowing through launders to direct chill casting operations, following scrap recycling, melting, alloying, refining (chlorination), settling, degassing (SNIFF, ALPUR, *etc.*) and metal filtration operations. Figure 13 shows a typical LiMCA II monitoring the quality of molten aluminum flowing through a launder to a bank of DC casters. In addition to liquid aluminum, LiMCA technology has also been developed for molten magnesium,[23,24,25] copper,[26] and steel.[27,28] In this section, some metallurgical applications of LiMCA system in molten metals are presented that include a study of settling phenomena in holding furnaces,[15] analyses of the dynamic process of liquid metal filtration,[16,17] studies on the grain refinement mechanism of TiB_2,[29] melt cleanliness measurement in aluminum-silicon casting alloys,[30] molten magnesium,[25] copper-beryllium alloys,[26] and steel in tundish.[27] Numerical studies on the feasibility of discrimination of particles of different conductivity or density by LiMCA system are also described.

A. *Settling Phenomena in Holding Furnaces*

Settling is a natural phenomenon that the operator can use for improving the cleanliness of molten aluminum without using any molten metal treatment device. However, the extra waiting period introduced by settling can become very expensive from a productive capacity point of view. Therefore, it is important to obtain a detailed evaluation of settling phenomena in casting furnaces, in order to optimize the settling time during furnace preparations.

As settling is a dynamic behavior, the use of the LiMCA technique makes precise monitoring of the evolution of inclusions level possible. Holding furnaces used in an aluminum cast house are refractory lined rectangular vessels holding a bath of molten aluminum, which is kept molten using gas-fired overhead burners. As such, the temperature at the surface of the molten bath is about 50 °C higher than the metal at the bottom, resulting in a strongly thermally stratified condition. The industry went to great lengths to promote metal cleanliness by allowing the inclusions a holding time of perhaps 60 minutes to allow them to settle to the bottom and sidewalls of furnace. By pouring molten metal from the upper layer of the bath, it was believed this would produce the cleanest metal. With the advent of LiMCA technology, it was found that this was not the case, in that the concentration of inclusions within the bath was practically uniform. Figure 14 illustrates the improvement in metal cleanliness with time in both stationary and tilting furnaces. It can be seen that there is no fundamental difference in behavior between tilting and stationary furnaces. As such, metal quality from a state-of-the-art tilting furnace was found to be no better intrinsically, than that from a stationary furnace, tapped from the bottom region of the bath. Subsequent modeling of the stratified flow revealed the presence of strong, thermal natural convection currents running down the sloping sidewalls of the furnace and was able to account for the relative uniformity levels within the bulk of the thermal stratified melt.

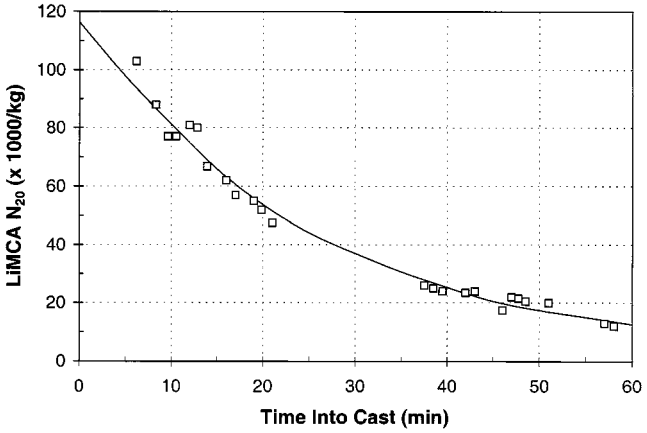

(*a*)

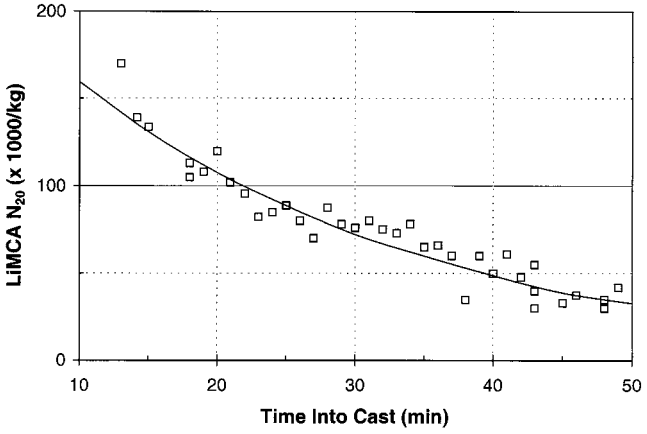

(*b*)

Fig. 14—Settling phenomena studied with LiMCA in aluminum holding furnaces: (*a*) stationary and (*b*) tilting.

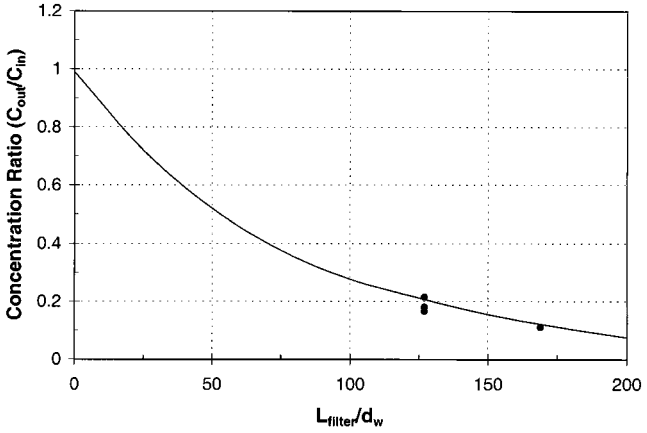

(*a*)

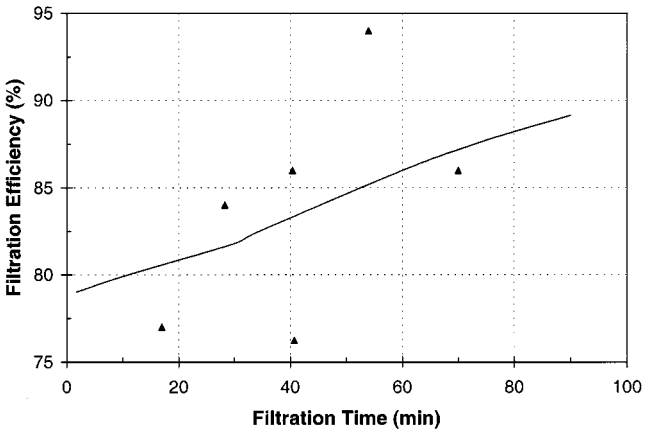

(*b*)

Fig. 15—(*a*) Comparison of predicted concentration ratio as a function of dimensionless filter thickness and (*b*) change in filtration efficiency in filter aging period with those obtained using LiMCA system in an industrial liquid aluminum filtration unit.

B. *Analyses of the Dynamic Process of Liquid Metal Filtration*

The filtration of liquid metals is now becoming a necessary refining step in the production of cleaner metals. This is especially true in the aluminum industry, where increasing demands for superior quality constantly lower the tolerance for nonmetallic inclusions. By filtering the liquid metal with some type of ceramic filter, the content of the nonmetallic inclusions can be substantially reduced. Evaluation of the performance of filters can be rather easily accomplished utilizing LiMCA analysis from a two-head system, *i.e.*, measuring immediately before and after the filter.

Figure 15 provides a comparison between the numerically predicted and experimentally obtained results on a ceramic foam filter (CFF). The filters used in the experiments were designated as 30 ppi (ppi stands for pores per linear inch) with an average effective porosity of about 83 pct. The average diameter of the filter webs, d_w, was about 0.3 mm. Agreement was achieved between the predicted values and those measured on the concentration ratio of inclusions with size around 50 μm at the inlet and the outlet of the filter as a function of filter length in the initial filtration stage (Figure 15(a)) and the change in filtration efficiency of inclusions greater than 20 μm during filter aging period (Figure 15(b)).

The deterioration in filtration efficiency that occurs

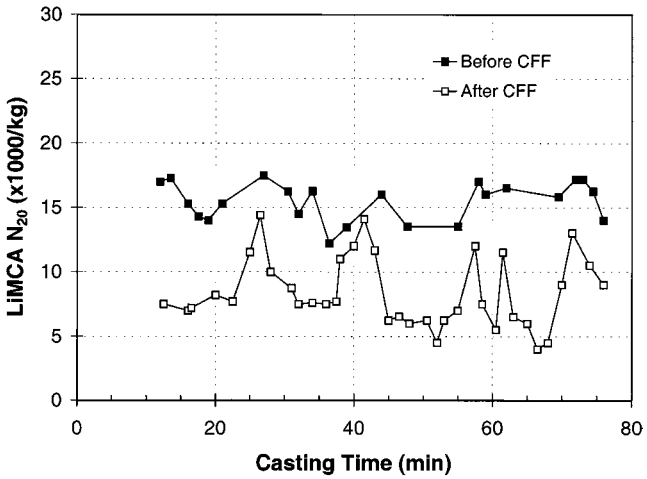

Fig. 16—Study of the dynamic performance of CFFs during casting with LiMCA system.

throughout casts can be measured by using LiMCA technology. Figure 16 shows the variations in metal cleanliness before and after filtration throughout a cast. It is seen that the metal quality was improved after filtration, however,

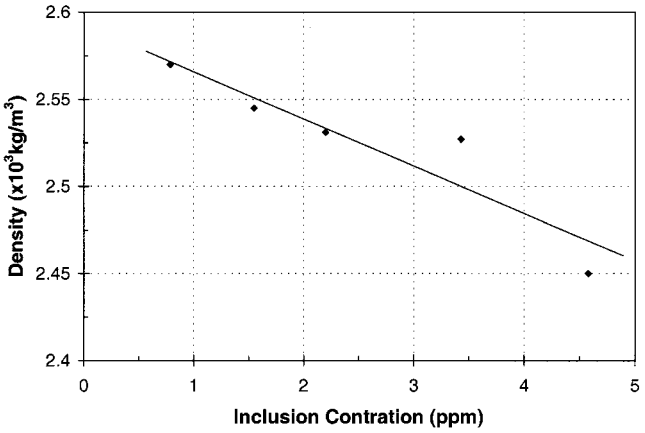

Fig. 17—Study of effect of inclusion concentration on the apparent density of reduced pressure samples with LiMCA system at a hydrogen level of 0.25 mL/100 g.

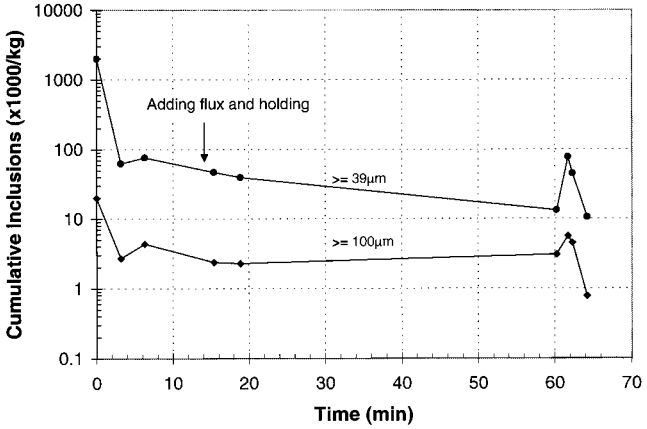

Fig. 18—Cumulative inclusions measured with LiMCA system in magnesium melts over the course of an hour long experiment.

inclusion release from the filter happened. This instability in the performance of CFFs appear more and more intensively as the cast proceeds.

C. *Studies on the Grain Refinement Mechanism*

The LiMCA has been applied to the analysis of grain-refining additions of titanium diboride (TiB_2) to aluminum-silicon casting alloys. Through DSP technology, it was conclusively demonstrated that TiB_2 additions to aluminum casting alloys, by themselves, have no grain-refining capability and can be recognized by the negative voltage pulses they generate when passing through the ESZ. The amplitude of the pulses is proportional to the size of TiB_2 particles and expressed in Eq. [11] of Part I. In the presence of excess titantium ($\cong$2 wt. pct), however, signals are positive, and grain-refining capability is observed. This observation confirms the hypothesis that a layer of $TiAl_3$ coats TiB_2 particles, which is needed for epitaxial growth of nucleating grains of aluminum. The $TiAl_3$ has a low electrical conductivity, rendering such coated TiB_2 particles essentially nonconducting.

D. *Melt Cleanliness Measurement in Aluminum-Silicon Casting Alloys*

Besides measuring melt cleanliness in the primary aluminum industry for high quality products, such as can stock, foil, anodizing, or lithographic sheet, LiMCA technology has also been applied to Al-Si foundry alloys. In Figure 17, the density of the reduced pressure test samples as a function of inclusion concentration of a typical aluminum-silicon alloy (A356) at a measured hydrogen level of 0.25 mL/100 g is plotted. It can be seen that the porosity of reduced pressure samples increases greatly with increased inclusion concentration at a constant level of dissolved hydrogen. In these experiments, the major types of inclusions observed in the A356 alloy (no grain refinement) were aluminum oxide (Al_2O_3) and magnesium-bearing compounds (Al_2MgO_2 and MgO). These inclusions generally have poor wettability with molten aluminum and may provide potential heterogeneous sites for pore nucleation. Certain local structural defects of oxide films and clusters, such as gaps, cracks, and concave interfaces, will further facilitate heterogeneous pore nucleation. Therefore, it can be expected that the porosity of a casting structure will increase proportionally as the total number of inclusions increases.

E. *Cleanliness Measurement in Molten Magnesium*

Liquid metal quality is becoming an important issue for the magnesium industry in terms of the recycling of return scrap for high-quality die casting and for effecting process improvements in the handling and refining of melts. Recently, a novel probe called concentric steel tube probe,[31] comprising a pair of spring-loaded concentric steel tubes separated by a ceramic orifice disc, has been tested successfully in the laboratories and pilot plant melting furnaces. One of the experiments was carried out using return scrap from cylinder head castings, chainsaw handles, casing covers, and similar materials. This experiment was prompted by the need to be able to recycle return scrap by the industry, given the rising demand for high quality magnesium die castings. Figure 18 shows typical laboratory results obtained over the course of an hour long experiment. Following immersion of the probe, 5 minutes was allowed for the inner tube to reach thermal equilibrium with the melt. During this time, argon was gently bubbled through the ESZ orifice, so as to keep it clear of any accumulated debris during initial immersion and subsequent holding. The first reading after this period indicated the cumulative presence of more than 1 million inclusions per kilogram of melt greater than 39 μm equivalent diameter, and more than 10,000 inclusions per kilogram of melt greater than 100 μm. Over the course of the next 20 minutes, the melt quality gradually improved. Extra flux was then added to clean the melt further, and measurement performed 40 minutes later indicated similar melt quality. Figure 19 shows the inclusion size distribution for four of the first samples drawn into the LiMCA system plotted in Figure 18. Assuming that all inclusions are magnesium oxides with the density of 3.65×10^3 kg/m^3, the weight content of inclusions within the melt can be deduced, which are 16.8 ppmw at a holding time of 3.16 minute, 28.8 ppmw at 6.31 minute, 15.9 ppmw at 15.4 minute, and 16.8 ppmw at 18.88 minute. These values are more than 4.5 times as high as a previously reported result obtained with the Porous

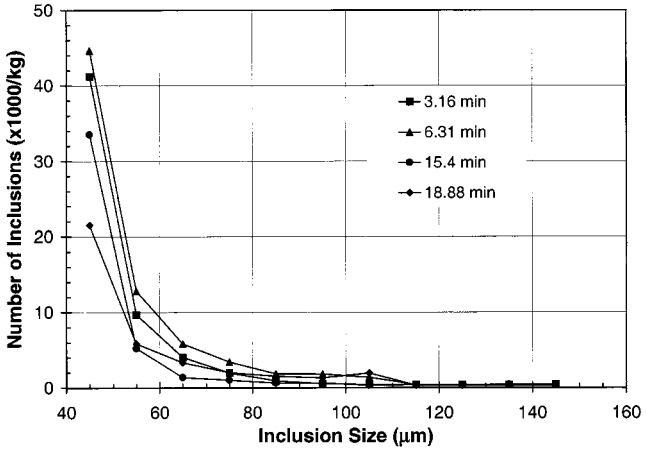

Fig. 19—Inclusion size distribution with the variation of holding times measured with LiMCA system in magnesium melts.

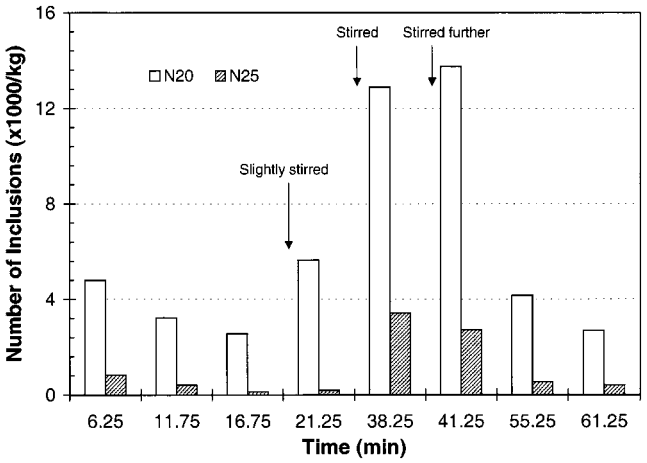

Fig. 20—Variation of number density of inclusions in Cu-Be alloy 25 with time measured with LiMCA system, before and after stirring.

Disk Filtration Analysis (PODFA) technique.[32] This would be due to the use of return scrap in LiMCA experiments, highly contaminated with oil, dust, paint, iron inserts, *etc.* while clean scrap in PODFA experiments.

F. *Melt Cleanliness Measurement in Copper-Beryllium Alloys*

Copper-rich beryllium alloys are heat treatable with important industrial applications where fatigue strength is a critical component of their combined set of properties, such as good corrosion and wear resistance and high thermal and electrical conductivity. The inevitable presence of beryllia particles within the alloy matrix can reduce fatigue life. It can also give rise to surface defects in thin sheet and strip products. A reduction in the number density, and size of oxide inclusions should, therefore, improve fatigue performance as in other alloy systems. Figure 20 shows the measured number densities of BeO particles *vs* time. Each measurement corresponds to a data acquisition period of 60 seconds and contains an estimated sample mass of 68 g. The figure gives a clear indication of the increase in the number density of particles caused by disturbing the metal surface with a graphite rod. Inclusion population densities dropped after prolonged periods of rest, confirming the importance of melt hydrodynamics and avoidance of surface disturbances.

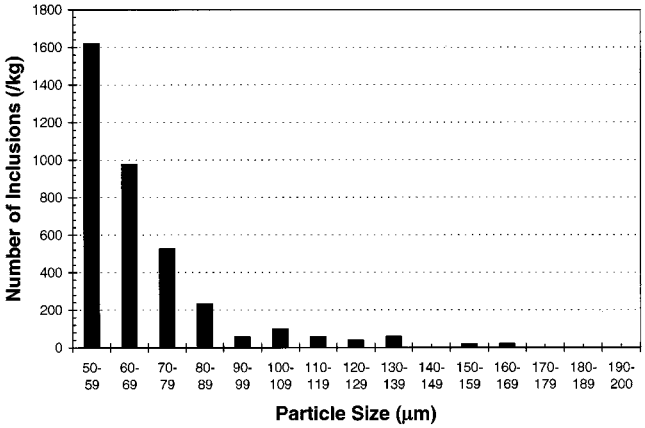

Fig. 21—Inclusion size distribution in steel melts in tundish measured with LiMCA system.

G. *Cleanliness Measurement in Liquid Steel*

After the successful application of LiMCA in aluminum industry, many efforts have been devoted to extend the technology to liquid steel. Plant tests to date have concentrated on aluminum-killed steels and interstitial-free steels and have proved successful. High silicon transformer grades are extremely easy and well behaved for ESZ experiments. In applying the inclusion sensor to an industrial setting, there are three possible monitoring locations of interest. The first is at the strong stir station when steel is held in the teeming ladle, the second in the tundish and as close to the exit ports as possible, and finally, within the mold of a caster just prior to solidification. Figure 21 shows the inclusion size distribution measured at the exit port of a 60 ton tundish, in which the number of inclusions per kilogram of steel is given in intervals of 10 micrometers. As compared with preliminary tests at McGill using 10 kg inductively stirred melts of aluminum-silicon killed steels where no particles greater than about 10 μm were typically sensed, the larger inclusions typically registered in the tundish were in the hundreds of micrometer diameter size range. One can speculate that many of these latter inclusions (which proved to be pure alumina) were the result of the turbulent entry of clean steel (containing much smaller inclusions) from the ladle shroud, combined with turbulent motions leading to migration of alumina inclusions toward the centers of eddying motions. Owing to their ferrophobic nature, adhesion and sintering could lead to the formation of the macroinclusions of alumina actually measured and observed in slime tests.

H. *Particle Discrimination in LiMCA System*

It would tremendously extend its applications if the LiMCA system can discriminate different types of inclusions in molten metals. In this section, numerical simulation will be carried out to prove LiMCA system can discriminate inclusions based on inclusion density and conductivity.

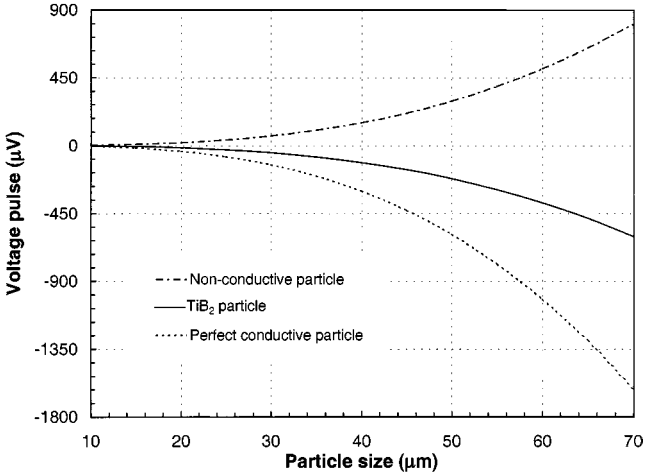

Fig. 22—The voltage pulse in molten aluminum as a function of the particle diameter.

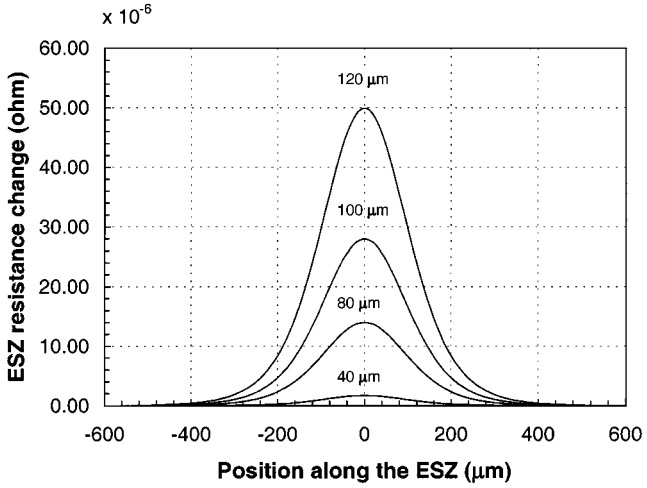

Fig. 23—ESZ resistance change with the position of nonconductive particles of various diameters in aluminum LiMCA system.

1. *Discrimination of conducting and nonconducting particles*

Conducting and nonconducting inclusions can be readily discriminated from one another as they generate negative and positive peak signals, respectively. The magnitudes of the signals, however, are different for particles of the same size but of different conductivity. Take the measurements in molten aluminum under typical operating conditions of a LiMCA system as examples, Figure 22 presents a plot of voltage pulse as a function of particle diameter, where the particles studied include nonconducting (Eq. [7] in Part I), perfectly conducting (Eq. [10] in Part I), and equivalent conducting to TiB_2 (Eq. [11] in Part I). It can be seen that the amplitude of the signals caused by perfectly conducting particles is twice that for nonconducting particles of the same size, while the amplitude for TiB_2 particles is predicted to be only three fourths of that of nonconducting particles of the same size.

2. *Discrimination of nonconducting particles of different density*

As discussed in Section III–D for APS II system, particle discrimination in LiMCA system seems feasible thanks to DSP technology. For every transient pulse generated when a particle passes through the ESZ, seven parameters are used to characterize the pulse, as shown in Figure 2. The study of particle discrimination in metal-based LiMCA systems followed the same methodology as that applied for the APS II system. Figure 23 shows the ESZ resistance variation as particles of different diameters pass through an orifice of 300 μm in molten aluminum under typical operating conditions. It can be seen that larger particles reach the noise threshold resistance further away from the orifice center than do smaller particles. Therefore, smaller particles travel shorter distances when transient times are measured by the LiMCA system. For example, a 100 μm particle reaches the noise threshold of 15 mV at 0.395 mm from the center of orifice, while it is 0.206 mm for a particle of 40 μm. Therefore, the transient time measured for a particle of 40 μm is the time it takes to travel 0.412 mm near the center of the orifice, while for a particle of 100 μm, it is the time to travel 0.79 mm.

To study the particle discrimination numerically, Eqs. [12] and [13] for the fluid flow and Eq. [19] for the motion of particles described in Part I were solved first for microbubbles and alumina particles of varying size flowing through the whole orifice. Since the effect of the entry point on the time the particles take to go through the physical length of the orifice without grazing the wall is very small (as shown in Figure 16 of Part I), an entry point of $y_P/R = 2$ was chosen for this study. Then, the transient time was obtained by considering the noise threshold of the LiMCA system, which is usually set as $\pm$ 15 mV. The results are shown in Figure 24.

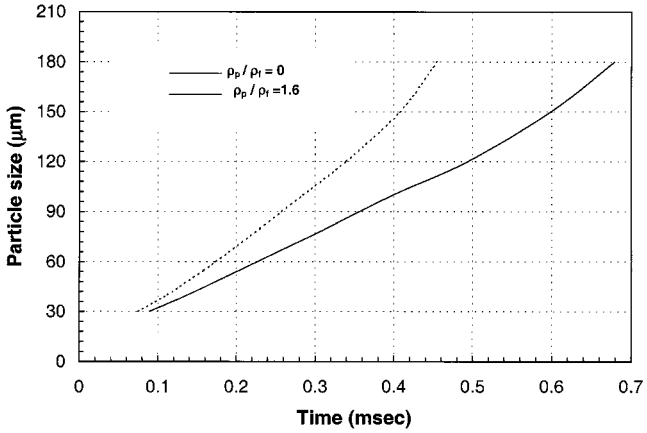

Fig. 24—Numerically predicted transient time *vs* particle size in aluminum LiMCA system.

It can be seen that bubbles have shorter transient times than do alumina particles of the same size, which can be explained by the different relative velocity developed when they move through the ESZ, as shown in Figure 13(a) of Part I. Bubbles, which lead the fluid flow in the axial direction, travel faster than alumina particles, which are denser than the liquid aluminum and, thus, lag behind the fluid flow when traveling within the ESZ.

It is also noted from Figure 24 that larger particles have longer transient times than smaller ones of the same density. This is easy to explain for alumina particles. For alumina particles, the larger the size, the lower the velocity. On the

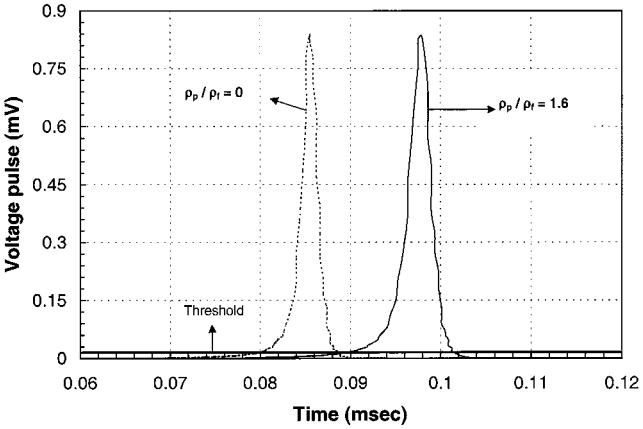

Fig. 25—Numerically predicted voltage pulse in aluminum LiMCA system.

other hand, for bubbles, the larger the size, the higher the velocity. However, because larger bubbles reach the voltage threshold much further away from the orifice center, resulting in a longer distance to travel, the transient time of larger bubbles appear to be larger than that of smaller bubbles. It was also found that the difference in transient times for bubbles, and alumina particles become more significant as particle size increases, improving the discrimination between particles of different densities.

Besides the transient time, on which particle discrimination can be carried out, pulse shape is also characteristic of different particles in the metal-based LiMCA system. Figure 25 shows the signal shapes for a microbubble and an alumina particle flowing into the ESZ from an entry point of $y_p/R = 2$. The bubble, which has a lower density, undergoes acceleration as it approaches the center of the converging ESZ, arriving more rapidly than the alumina particle of higher density and inertia, which accelerates more slowly.

V. CONCLUSIONS

The mathematical model developed in Part I was used to study the performance of the probes in the water-based APS II and the metal-based LiMCA systems. The results show that the currently used parabolically shaped orifice is favorable for particle detection by providing a uniform and stable flow field and a parallel- distributed electric current at the throat of the orifice. Combined with the Ohmic model of the ESZ, which correlates the ESZ resistance change with particle position within the ESZ, the model predicts that larger particles have longer transient times than do smaller ones, that less denser particles have shorter transient times than do more denser particles of the same size in water and metal based LiMCA systems. The particle diameter can be estimated from the peak height. Then, given the known particle diameter, the transient time is a function of the density difference alone for a given operating condition. Differences in transient times become more pronounced the larger the inclusions, in keeping with experimental data. In the metal-based LiMCA system, conducting and nonconducting inclusions can be readily discriminated from one another as they generate negative and positive peak signals, respectively. The results prove that inclusion discrimination on the basis of particle density difference is realizable in a water-based LiMCA system, and, from a theoretical standpoint, that particles of different density and conductivity in molten metals are potentially distinguishable with a LiMCA system using DSP technology. Applications of the APS II system are described, including the physical modeling of inclusion distributions in stirred ladles, inclusion float out in steelmaking tundishes, and submerged powder injection for the refining and alloying of melts. Some metallurgical applications of the metal-based LiMCA system are presented including study of the settling phenomena in aluminum holding furnaces, analyses of the dynamic process of liquid metal filtration, the study of the grain-refinement mechanism of TiB_2 for aluminum melts, and finally, melt cleanliness measurements in aluminum-silicon casting alloys, in molten magnesium, in copper-beryllium alloys, and in steel in tundishes.

SYMBOLS

C_{in}	concentration of suspended inclusions at inlet (kg^{-1})
C_{out}	concentration of suspended inclusions at outlet (kg^{-1})
d_w	average diameter of filter webs (m)
E	electromotive force of a battery (V)
h	height position in cylindrical ladle
H	ladle height
h_b	bubble penetration depth in the building type of powder injection regime
I_0	electric current inside an ESZ in the absence of a particle (A)
J_{max}	disengagement distance in powder injection processes
L_{filter}	length of a filter (m)
N_{20}	number of inclusions of size greater or equal to 20 μm (kg^{-1})
N_{25}	number of inclusions of size greater or equal to 25 μm (kg^{-1})
N_{in}	number density of inclusions per unit volume at the inlet of a tundish
N_{out}	number density of inclusions per unit volume at the outlet of a tundish
Q	volumetric gas flow rate
r	radial position in a cylindrical ladle
R_{AB}	electrical resistance between the electrodes without a particle (ohm)
R_B	ballast resistance (ohm)
ΔR_{AB}	electrical resistance increase generated by the passage of a particle (ohm)
R_{ladle}	radius of a cylindrical ladle
u_s	Stokes velocity of an inclusion
V_{AB}	electrical potential between the electrodes without a particle (V)
ΔV_{AB}	electrical potential increase generated by the passage of a particle (V)

REFERENCES

1. W.H. Coulter: U.S. Patent 2,656,508, 1953.
2. G. Carayannis, F. Dallaire, X. Shi, and R.I.L. Guthrie: *Symp. Artificial Intelligence in Materials Processing Operations*, Edmonton, AB, Canada, 1992, pp. 227-44.
3. *Aqueous Particle Sensor System-User's Manual*, McGill Metals Processing Center, McGill University, Montreal, 1996.

4. Xiaodong Shi: Master's Thesis, McGill University, Montreal, 1994.
5. R.I.L. Guthrie: *Proc. Int. Symp. on Computer Applications in Metallurgy and Materials Processing*, Calgary, AB, Aug. 16-19, 1998, pp. 2-18.
6. R.W. Beblois and C.P. Bean: *Rev. Scientific Instrum.*, 1970, vol. 41, pp. 909-15.
7. W.R. Smythe: *Phys. Fluids*, 1961, vol. 4, pp. 756-59.
8. R.W. Deblois, C.P. Bean, and R.K.A. Wesley: *J. Coll. Interface Sci.*, 1977, vol. 61, pp. 323-35.
9. S. Kuyucak, H. Nakajima, and R.I.L. Guthrie: *Proc. 5th Int. Iron & Steel Congr.*, 1986, pp. 193-98.
10. S. Joo and R.I.L. Guthrie: *Metall. Trans. B*, 1993, vol. 24B, pp. 755-65.
11. G. Yamanoglu, R.I.L. Guthrie, and D. Mazumdar: *Can. Metall. Q.*, 1999, vol. 38 (1), pp. 61-80.
12. C. Carozza: Master's Thesis, McGill University, Montreal, 1999.
13. C. Dupuis and R. Dumont: *Light Met.*, 1993, pp. 997-1002.
14. J.P. Martin, G. Dube, D. Frayce, and R.I.L. Guthrie: *Light Met.*, 1988, pp. 445-55.
15. D. Doutre, G. Dube, B. Gariepy, and J.P. Martin: *Light Met.*, 1985, pp. 1179-95.
16. C. Tian and R.I.L. Guthrie: *Metall. Mater. Trans. B*, 1995, vol. 26B, pp. 537-46.
17. C. Tian and R.I.L. Guthrie: *Light Met.*, 1995, pp. 1263-72.
18. L.A. Strom, J.W. Black, R.I.L. Guthrie, and C. Tian: *Light Met.*, 1992, pp. 1093-1100.
19. N.J. Keegan, W. Schneider, H.P. Krug, and V. Dopp: *Light Met.*, 1997, pp. 973-82.
20. E.U. Comerford, L.G. Hudson, and G. Beland: *Light Met.*, 1994, pp. 1083-91.
21. C. Tian and R.I.L. Guthrie: *Light Met.*, 1993, pp. 1003-07.
22. J.P. Martin and F. Painchaud: *Light Met.*, 1994, pp. 915-20.
23. R.I.L. Guthrie: U.S. Patent 5,789,910, 1998.
24. C. Carozza, P. Lenard, R. Sankaranayanan, and R.I.L. Guthrie: *Light Met.*, 1997, pp. 185-96.
25. R.I.L. Guthrie, M. Li, and J.Y. Buyan: *Proc. 1st Israeli Int. Conf. on Magnesium Science and Technology*, Dead Sea, Israel, Nov. 10–12, 1997, pp. 81-87 (Keynote Address).
26. S. Kuyucak and R.I.L. Guthrie: *Can. Metall. Q.*, 1989, vol. 28, pp. 41-48.
27. R.I.L. Guthrie and H.C. Lee: *Proc. Steelmaking Conf.*, 1992, pp. 799-805.
28. S. Kuyucak, H. Nakajima, and R.I.L. Guthrie: *Proc. 6th Process Technology Conf.*, 1986, pp. 193-98.
29. P.S. Mohanty, R.I.L. Guthire, and J.E. Gruzleski: *Light Met.*, 1995, pp. 859-68.
30. X.G. Chen, R.I.L. Guthrie, and J.E. Gruzleski: *Proc. 4th Int. Conf. on Molten Aluminum Processing*, 1995, pp. 15-28.
31. R.I.L. Guthrie: U.S. Patent 5,789,910, 1998.
32. P. Bakke, J.A. Laurin, A. Provost, and D.O. Karlsen: *Light Met.*, 1997, p. 1019.